# Parametric stochastic 3D model for the microstructure of anodes in lithium-ion power cells

Daniel Westhoff[a,*], Julian Feinauer[a,b], Klaus Kuchler[a], Tim Mitsch[b], Ingo Manke[c], Simon Hein[d,e,f], Arnulf Latz[d,e,f], Volker Schmidt[a]

[a] *Ulm University, Institute of Stochastics, Helmholtzstr. 18, 89069 Ulm, Germany*
[b] *Deutsche ACCUMotive GmbH & Co. KG, Neue Straße 95, 73230 Kirchheim unter Teck, Germany*
[c] *Helmholtz-Zentrum Berlin, Institute of Applied Materials, Hahn-Meitner-Platz 1, 14109 Berlin, Germany*
[d] *Institute of Engineering Thermodynamics, German Aerospace Center, Pfaffenwaldring 38-40,70569 Stuttgart, Germany*
[e] *Helmholtz Institute for Electrochemical Energy Storage, Helmholtzstraße 11, 89081 Ulm, Germany*
[f] *Institute of Electrochemistry, Ulm University, Albert Einstein-Allee 47, 89081 Ulm, Germany*

**Abstract**

The microstructure of anodes in lithium-ion batteries has a strong influence on their electrochemical performance and degradation effects. Thus, optimizing the morphology with respect to functionality is a main goal in battery research. Doing so experimentally in the laboratory causes high costs with regard to time and resources. One way to overcome this problem is the usage of parametric 3D microstructure models, which allow the realization of virtual morphologies on the computer. The functionality of microstructures generated with such models can be investigated by means of numerical transport simulations. The results of this procedure, which is called virtual materials testing, can be used to design anodes with improved morphologies that lead to a better electrochemical performance. Recently, a particle-based stochastic microstructure model for anodes in lithium-ion energy cells has been proposed. In the present paper, an extension of this model to describe the morphology of anodes in power cells, whose structure strongly differs from energy cell anodes, is introduced. The extensions

*Corresponding author
*Email address:* daniel.westhoff@uni-ulm.de (Daniel Westhoff)

include techniques to model anisotropic morphologies with a low volume fraction of the particle phase and strongly irregular particle shapes. The model is fitted to 3D image data of a power cell anode and validated using morphological image characteristics. Furthermore, we show examples of modifications of our microstructure model that can be made for generating further virtual morphologies. Finally, we briefly explain how electrochemical characteristics can be estimated using thermodynamically consistent transport theory. To illustrate this, we compute the cell potential over time during lithiation for image data of real microstructures as well as corresponding microstructures simulated by our model.

*Keywords:* stochastic microstructure modeling, power cell, lithium-ion battery, anodes, spherical harmonics, anisotropy

## 1. Introduction

Lithium-ion batteries have a wide field of applications, ranging from small mobile devices up to large-scale applications, e.g., in electric vehicles. However, there are still unresolved problems concerning capacity, power, safety, duration and ageing effects, see, e.g., [1, 2, 3, 4]. For an overview of challenges regarding lithium-ion batteries we refer to [5].

It is well known that the morphological properties of the electrodes strongly contribute to these problems. Thus, the microstructure of anodes and cathodes is of high interest in battery research [6, 7, 8]. Many theoretical investigations are based on the famous model introduced by Newman [9]. However, Newman's model does not take into account the full 3D information of the microstructure. This can be overcome using microstructure-resolved transport models, see [10]. Given the 3D morphology of the electrodes, such models can be used to predict the electrochemical performance of battery cells. Thus, if a tool is on hand that systematically generates virtual 3D microstructures with varying morphological properties, microstructure-resolved transport models can be used to identify electrochemically preferable structures, a procedure called virtual materials test-

ing. Stochastic microstructure modeling has proven to be an ideal tool for the generation of such structures for various energy materials, see, e.g., [11, 12]. In particular, virtual materials testing based on stochastic modeling has been performed in [13] and [14] for a wide class of 3D structures, which are closely related with microstructures observed in tomographic image data for electrodes of solid oxid fuel cells (SOFC). Thus, it is desirable to develop a parametric stochastic model that is capable of creating a broad range of battery electrode morphologies, which can be used as input for microstructure-resolved transport models. By doing so, an efficient tool (compared to experimental manufacturing and testing of electrodes in the laboratory) to identify preferable structures is provided.

Depending on the application of a battery, either power cells or energy cells are used. While for an energy cell the capacity is of high priority, which is reflected in a high volume fraction of the particle phase, for power cells a fast ion transport is necessary for high charge and discharge currents, and therefore the volume fraction of the pore phase needs to be rather high. For a discussion of the morphological differences between energy and power cells we refer to [15].

Recently, a parametric stochastic model for the microstructure of anodes in energy cells has been developed [16]. The model is particle-based, and each particle is modeled using so-called spherical harmonics [17]. The particles are placed in a system of convex polytopes that forms a decomposition of the region of interest. Due to the high volume fraction of the particle phase in energy cell anodes, it is easily possible to force each particle to touch a previously chosen subset of neighbors, in a way that the whole 3D structure is completely connected.

In the present paper, a parametric stochastic microstructure model for power cell anodes is introduced, which is based on the approach considered in [16]. The model accounts for the lower volume fraction of the particle phase, but still ensures its complete connectivity. In addition, techniques for modeling particles with more irregular shapes (compared to [16]) as well as anisotropy of the particle phase (which results from the calendering process) are presented.

We fit the model to tomographic 3D image data (which we will call 'real data set' or just 'real data' in the following) of a power cell anode and compare morphological characteristics between real and simulated data.

In addition, we show various kinds of modifications of the microstructure that can be realized by the model. Finally, we briefly discuss how the thermodynamically consistent transport theory developed in [10] can be applied to image data of real microstructures and virtual ones generated by the model. To give an example, we compute the cell potential over time during lithiation of the electrode. Those two aspects (the ability to generate virtual, but still realistic structures and to perform electrochemical simulations) provide the basis for virtual materials testing.

The paper is organized as follows. In Section 2, a brief overview of the considered material and data preprocessing steps is given. The stochastic microstructure model as well as the fitting procedure to real data are introduced in Section 3. The validation based on morphological image characteristics is shown in Section 4. An outlook towards virtual materials testing is given in Section 5. In Section 6, the results are summarized and possible further work is discussed.

## 2. Material Description and Data Preprocessing

The real data, to which the model is applied, is taken from a plug-in hybrid vehicle's battery cell. The cells have been exposed to moderate cyclic aging, i.e., no too strong structural changes due to aging are expected. The imaging was performed at a synchroton X-Ray facility (BAMLine, BESSY, Berlin). For details regarding the imaging process, we refer to [18], where the technique has been introduced in detail. The imaging procedure resulted in an 8-bit 3D grayscale image with $1601 \times 1401 \times 109$ voxels, where the voxel size is $0.44\ \mu\text{m}^3$.

This grayscale image is binarized, i.e., each voxel is either assigned to the particle phase or to the complementary phase, the pore phase. First, in order to remove noise in the image data, a Gaussian filter (see, e.g., [19]) with parameter

$\sigma = 1$ is applied. After that, a (manually chosen) global threshold of 34 is applied, as this value leads to the best binarization considering visual comparison. We expect the particles not to have holes, however, due to artifacts in the data, after binarization, some holes are visible. Those holes are detected using the Hoshen-Kopelmann clustering algorithm [20] and removed, i.e., the corresponding voxels are assigned to the particle phase. This is done for clusters found up to a size of 10000 voxels. Finally, as we expect the particle phase to be completely connected, a clustering algorithm is performed (now on the particle phase) and only the largest cluster (and clusters touching the edge of the image, as their connectivity across the border is not known) are kept, which removes a few artifacts in the background.

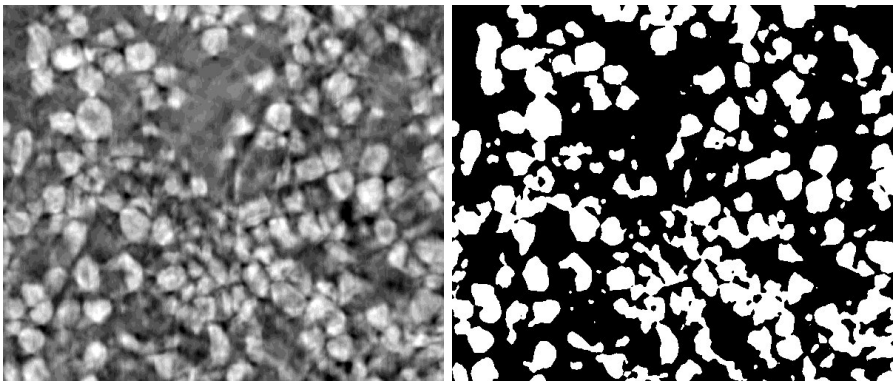

(a) Grayscale image. (b) Corresponding binarization.

Figure 1: 2D planar cutout of the real data set.

As an example, Figure 1 shows a cutout of a 2D slice from the grayscale image and the corresponding binarization. The complete binarized 3D data set is visualized in Figure 2.

As the parametric stochastic model is particle-based, we need a segmentation of the binary image that allows identification of individual particles. This is necessary for parameter estimation, see Section 3.4. The segmentation is done using a watershed algorithm, see, e.g., [21] for detailed information. The algorithm is adapted from [22] and is based on so-called regional local minima, which

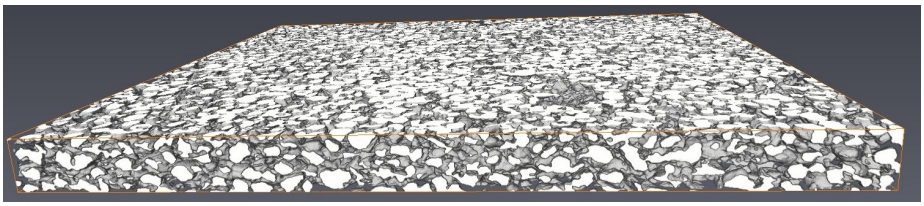

Figure 2: 3D rendering of the binarized data set.

extend the concept of simple local minima in order to prevent oversegmentation. We consider the so-called negative Euclidean distance transformation of the binary image, i.e., the value of each voxel is given by the negative of its shortest Euclidean distance to the pore phase. Based on this grayscale image, the markers for the watershed algorithm are chosen as described in [22]. In Figure 3 a cutout of the segmented image is displayed.

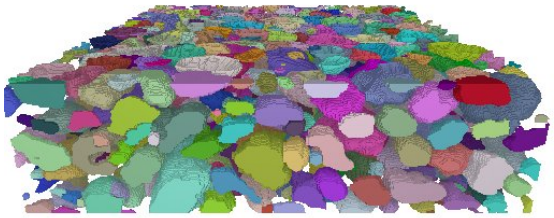

Figure 3: 3D rendering of a cutout of the image after segmentation; each particle is labeled using a different color.

Given the segmentation of the binary image, we have all the structural information we need to fit the parametric stochastic model to this data set. The results will be discussed in Section 4, after introducing the principle ideas of the model in Section 3.

## 3. Parametric Stochastic Microstructure Model

The construction of the stochastic model consists of several steps. An overview of the modeling approach is given in Figure 4 as a 2D sketch.

To begin with, a random marked point pattern that mimics the positions of

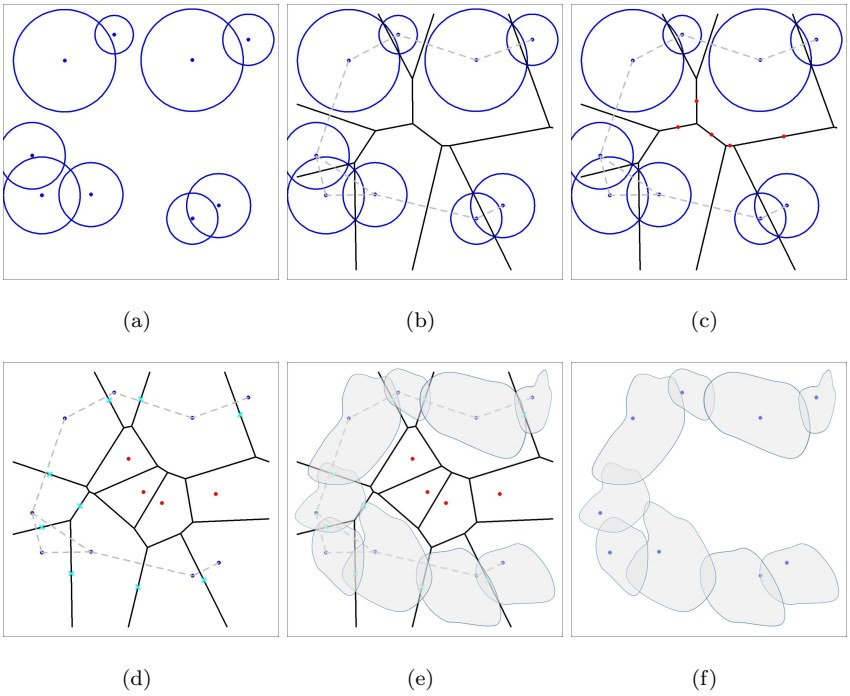


Figure 4: Overview of the modeling idea. (a) A random marked point pattern is realized (blue dots and circles); (b) An anisotropic connectivity graph (dashed grey lines) based on the Laguerre tessellation (black lines) induced by the random marked point pattern is simulated; (c) Candidates for marked points (red dots) that induce empty polytopes (i.e., where no particle is placed) are created; (d) Only those candidates are accepted the corresponding polytopes of which do not cover the center of Laguerre facets between two particles that are supposed to be connected (lightblue); (e) Particles are created in the polytopes that are induced by blue dots using spherical harmonics; (f) The auxiliary tools are deleted and only the union of particles is kept.

particles and their approximate sizes is simulated, see Figure 4(a), where the mark is indicated as radius of a circle around the corresponding point. Using a so-called Laguerre tessellation (see [23] for details), each of these marked points induces (under some regularity conditions, which are usually fulfilled for the kind of point pattern considered in this work) exactly one convex polytope. These polytopes are shown with black lines in Figure 4(b). In each of them a particle will be placed. But beforehand, we have to indicate which particles should be connected, ensuring full connectivity of the particle system. Therefore, a connectivity graph is constructed, where the connection probability between two particles depends on a) the surface area of the facet between their corresponding polytopes, b) the distance of (seed) points and c) the angle between a horizontal plane and the line between the two marked points inducing the corresponding polytopes. Note that by including the angle as a connection criterion for the connectivity graph, anisotropy can be included into the model, i.e., particles can be stretched and preferably connected in a specific direction. In Figure 4(b) the connectivity graph is shown with dashed grey lines. Anisotropy of the graph is indicated in horizontal direction. Now, we have a system of convex polytopes, where we want to put one particle into each polytope, following the connectivity constraints given by the connectivity graph. However, to account for the low volume fraction of the particle phase in power cell anodes, we have to shrink the sizes of polytopes. Otherwise the connectivity induced by the graph cannot be achieved with reasonably shaped particles. Thus, candidates for marked points that induce empty polytopes (i.e., where no particle is placed) are added to the marked point pattern that induces the Laguerre tessellation, see the red points in Figure 4(c). From these candidates, only those points are chosen, the corresponding polytopes of which (if added to the generators of the Laguerre tessellation) do not cover the center of a Laguerre facet between two polytopes whose particles are supposed to be connected (lightblue in Figure 4(d)). Given the connectivity graph and the final tessellation (Figure 4(d)), particles are placed in each polytope of the initial point pattern, which are now shrinked because the polytopes induced by the additional points cover some fraction of

space, see Figure 4(e). The particles are forced to fulfill the conditions induced by the connectivity graph, i.e., touch a subset of surrounding particles. Finally, only the particle system is kept (Figure 4(f)) and a morphological closing is performed.

In the following subsections, each step of the model construction is described in detail.

### *3.1. Modeling the particle positions and approximate sizes*

To begin with, a random marked point pattern depicting particle positions and approximate sizes is realized. Figure 5(a) shows a representation of a cutout of real data as spheres with volume-equivalent radii, i.e., for each particle with center of mass $m$ and volume $V$, a sphere with midpoint $m$ and radius $\sqrt[3]{3V/4\pi}$ is shown. This results in a system of (slightly) overlapping spheres. Thus, we found

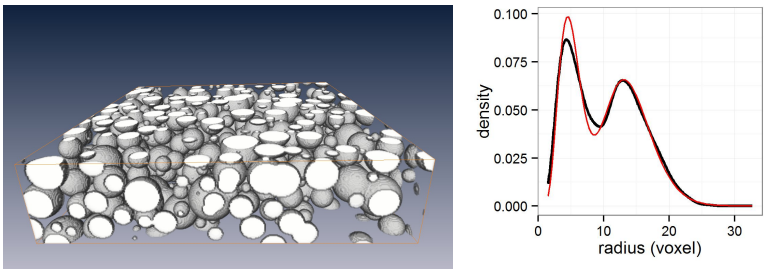


(a) Cutout of real particle system represented as spheres with volume-equivalent radii.

(b) Distribution of radii (estimated from data in black, fitted mixed gamma distribution in red).

Figure 5: Representation of particles by volume equivalent radii.

that a collective rearrangement algorithm is useful for modeling this pattern. Such algorithms are, e.g., used for modeling packings of spheres, see [24]. Here, first we fit a parametric probability distribution to the empirical distribution of the volume-equivalent radii observed in real data. A mixed gamma distribution gives a good fit as can be seen in Figure 5(b), i.e., the radii approximately follow a gamma distribution with shape parameter $p_1 > 0$ and scale parameter $b_1 > 0$

with some probability $\alpha$, where $0 < \alpha < 1$, and another gamma distribution with parameters $p_2 > 0$ and $b_2 > 0$ with probability $1 - \alpha$. Then, we use a homogenous Poisson point process with some intensity $\lambda > 0$ to model the initial configuration for the collective rearrangement, as the Poisson process is one of the easiest models for random allocation of points. For details about point processes, we refer to [25]. Let $\{S_i, i \in \mathbb{N}\}$ be a measurable indexing of the homogenous Poisson point process. Each point $S_i$ is marked with a radius $R_i$ drawn from the mixed gamma distribution introduced above, resulting in an independently random marked point pattern $\{(S_i, R_i), i \in \mathbb{N}\}$, that can be interpreted as a system of spheres $\{\mathsf{S}(S_i, R_i), i \in \mathbb{N}\}$, where $\mathsf{S}(m, r)$ is a sphere with midpoint $m$ and radius $r$.

We want to simulate particle systems in a bounded sampling window $W \subset \mathbb{R}^3$. To avoid edge effects, we perform the simulations on a slightly larger sampling window $\widetilde{W} \supset W$. In the following, we consider the point pattern $\{(S_i, R_i), S_i \in \widetilde{W}\}$ and the corresponding sphere system $\{\mathsf{S}(S_i, R_i), S_i \in \widetilde{W}\}$. This is the initial configuration for the collective rearrangement algorithm, which is performed as follows.

1. For each sphere $\mathsf{S}(S_i, R_i)$, calculate the random force
$$F_i = \sum_{j:S_j \in \widetilde{W}} (S_i - S_j) \mathbb{1}_{\{R_j + R_i > ||S_i - S_j||\}},$$
where $\mathbb{1}_A$ is the indicator of the event $A$, i.e., $\mathbb{1}_A = 1$ if $A$ occurs, and otherwise $\mathbb{1}_A = 0$, and $||a - b||$ is the Euclidean distance between two vectors $a$ and $b$. This means, for each sphere that intersects $\mathsf{S}(S_i, R_i)$, we consider the vector from its centroid to $S_i$, and sum up all these vectors.
2. For each sphere $\mathsf{S}(S_i, R_i)$, calculate the mean random overlap $\bar{O}_i$ with all spheres it intersects, i.e.
$$\bar{O}_i = \frac{\sum_{j \neq i} (R_j + R_i - ||S_i - S_j||)\} \mathbb{1}_{\{R_j + R_i > ||S_i - S_j||\}}}{\#\{j : R_j + R_i > ||S_i - S_j||, j \neq i\}},$$
where $\#M$ is the number of elements in the set $M$.
3. If the mean of all mean overlaps $\bar{O}_i$ is larger than a given threshold $O_{thr}$, shift all $S_i$ by $F_i/||F_i||$ and go to step 1. Otherwise terminate.

Note that the force $F_i$ is a vector that shifts $(S_i, R_i)$ such that the overlap with neighboring spheres becomes smaller. By scaling it to unit length in Step 3 of the algorihm we ensure convergence to a state where a mean overlap of approximately $O_{thr}$ is achieved, avoiding uncontrolled large shifts. Thus, the algorithm yields a system of slightly overlapping spheres as desired. In the following, we call the resulting marked point pattern $\mathcal{S}_1 = \{(S_i, R_i),\, S_i \in \widetilde{W}\}$. The model validation performed in Section 4.1 will show that this model nicely fits the marked point pattern induced by the real data set.

The parameter $\lambda$ is chosen such that it resembles the intensity estimated from the point pattern induced by the particle centers in the real data set. We found that $\widehat{\lambda} = 4.87 \cdot 10^{-5}$. Note that the collective rearrangement algorithm does not change the intensity and thus we can control the final intensity of the point pattern.

The parameters for the mixed gamma distribution were estimated using expectation maximization as implemented in the *mixtools* package [26] in R [27]. We found that $\widehat{\alpha} = 0.43, \widehat{b_1} = 0.66, \widehat{p_1} = 7.81, \widehat{b_2} = 0.91$ and $\widehat{p_2} = 15.44$. The threshold $O_{thr}$ is chosen as the mean of all mean overlaps in the real data set (where particles are represented as spheres with volume-equivalent radii). This is 2.09 voxel length for our data set.

### *3.2. Modeling the connectivity graph*

In the previous step, we have modeled locations and approximate sizes of particles. Now, a connectivity graph is simulated that indicates which particles are supposed to be connected. A graph $G = (\mathcal{V}, \mathcal{E})$ consists of a set of vertices $\mathcal{V}$ and a set of edges $\mathcal{E} \subset \mathcal{V} \times \mathcal{V}$, where $\mathcal{V}$ can be seen as a set of points in some space (of sites) and $\mathcal{E}$ can be considered as segments connecting (some) pairs of points. For details regarding graphs, we refer to [28]. In our case, the vertices are the marked points considered in Section 3.1, i.e., $\mathcal{V} = \mathcal{S}_1$, and an edge between two marked points indicates that the corresponding particles are supposed to be connected.

As already mentioned, particles will be placed in convex polytopes, given by

a so-called Laguerre tessellation on the sampling window $\widetilde{W}$. Note that again the edge correction (i.e., considering the extended sampling window $\widetilde{W} \supset W$) is important to avoid boundary effects. Let $\mathcal{T}'$ be the Laguerre tessellation induced by the point pattern $\mathcal{S}_1$. Then $\mathcal{T}' = \{P'_i,\, S_i \in \widetilde{W}\}$ is a collection of convex polytopes, where $P'_j$ is the convex polytope corresponding to $(S_j, R_j) \in \mathcal{S}_1$. Furthermore, let $F'_{jk}$ be the joint facet of two neighboring polytopes $P'_j$ and $P'_k$. If $P'_j$ and $P'_k$ are not neighbors, then we put $F'_{jk} = \emptyset$. Note that this is not yet the final tessellation into which particles will be placed (as we want to include polytopes where no particle is placed), but we need the tessellation desribed above to construct the connectivity graph.

Of course, the connectivity graph should depend on the underlying tessellation, as it determines the rough shape of the particles. In particular, as it has been done in [16], particles should be connected with higher probability if the Laguerre facet between their polytopes is large, i.e., the particles placed in the polytopes induced by $(S_i, R_i)$ and $(S_j, R_j)$ should be connected with high probability if $F'_{ij}$ is large. Furthermore, the connection probability should decrease with increasing distance of particle seed points. Additionally, by the aid of the connectivity graph, we want to account for the anisotropic structure of the real data set.

To get an idea for modeling the connectivity graph, we analyze the real data set. We have already identified individual particles by segmentation techniques, see Section 2. Based on this, we can determine which particles are connected (which is the case if a voxel from one particle neighbors a voxel belonging to the other particle). Let furthermore $\mathcal{T}^{\exp}$ be the Laguerre tessellation induced by the marked point pattern $\{(s_i^{\exp}, r_i^{\exp}), i \in \{1, ..., n\}\}$, where $n$ is the number of particles extracted from the real data set, $s_i^{exp}$ is the barycenter of the $i-$th particle and $r_i^{exp}$ the corresponding volume-equivalent radius. Using this, we can estimate the probability $\widehat{P}_{\text{area}}(a)$ of two particles with barycenters $s_i^{\exp}$ and $s_j^{\exp}$ being connected, given that the area of the facet $f_{i,j}^{\exp}$ of $\mathcal{T}^{\exp}$ separating $s_i^{\exp}$ and $s_j^{\exp}$ is equal to $a$. The results obtained for the considered set of real

data are shown in Figure 6(a), black line. It can be nicely seen that the probability of connection increases with increasing facet area. For modeling purposes, a parametric curve (red) is fitted. The same procedure is performed considering the distance between two particle centers, i.e., $\widehat{P}_{\text{dist}}(d)$ is the estimated probability of two particles being connected, given that the distance between their barycenters is $d$ (and that their corresponding polytopes share a common facet), see Figure 6(b).

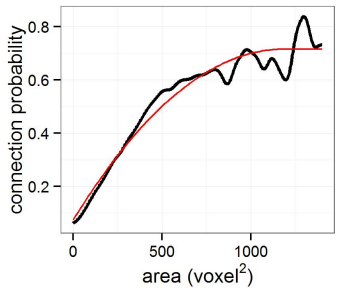


(a) Connection probabilites depending on the area of the joint facet of corresponding Laguerre polytopes.

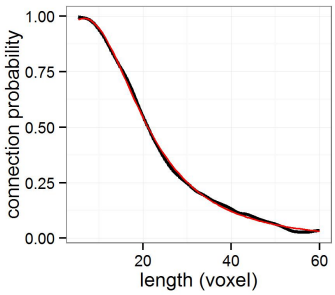


(b) Connection probabilites depending on the distance between barycenters.

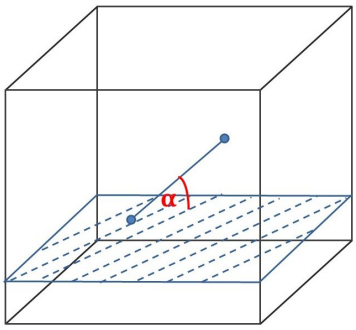


(c) Illustration of angle $\alpha$ (dots correspond to barycenters of two particles).

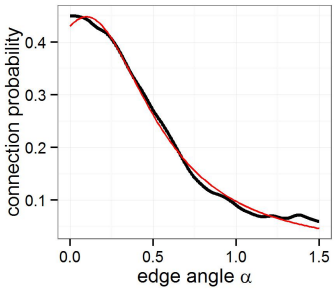


(d) Connection probabilites depending on the angle $\alpha$ between a horizontal plane and the segment between barycenters.

Figure 6: Probability of two particles being connected. Black: Estimated from real data set; Red: Parametric fit.

As already mentioned, we want to include the anisotropy information into the model using the connectivity graph. Therefore, similar to the criteria discussed above, we consider still another property of two particle centers - the angle $\alpha$ between a horizontal plane and the segment between the two particle centers, see Figure 6(c). In Figure 6(d) the probability $\widehat{P}_{\text{angle}}(\alpha)$ of two particles being connected, given that the angle between their barycenters is equal to $\alpha$, is shown. It can be seen that the probability of connection is larger for small angles - i.e., particles are rather connected horizontally than vertically. By including this when modeling the connectivity graph, we achieve two things. On the one hand, of course, we resemble exactly this property observed in the real data set in our model. But, on the other hand and even more important, this results in particles that are stretched in horizontal direction, because of the conditions (induced by the connectivity graph) they have to fulfil, i.e., the particles they have to touch. Thus, anisotropy is included into the model.

As already shown in Figure 6, we fit parametric curves to the empirical probability functions estimated from real data. The fitting is performed using the curve fitting tool in Matlab [29]. For the dependence on the area of the connecting facet, we have

$$P_{\text{area}}(a) = \min\{a_{\text{area}}a^2 + b_{\text{area}}a + c_{\text{area}}, 0.7161\}$$

where $a_{\text{area}} = -4.54 \cdot 10^{-7}$, $b_{\text{area}} = 0.0011$ and $c_{\text{area}} = 0.07503$. Note that 0.7161 is the maximum of this function on $\mathbb{R}_+$. Furthermore, it holds

$$P_{\text{dist}}(d) = \max\left\{\frac{a_{\text{dist}}d + b_{\text{dist}}}{d^2 + c_{\text{dist}}d + d_{\text{dist}}}, 0\right\}$$

where $a_{\text{dist}} = -3.14$, $b_{\text{dist}} = 279.8$, $c_{\text{dist}} = -16.29$ and $d_{\text{dist}} = 325.6$. For the angle, we have

$$P_{\text{angle}}(\alpha) = \frac{a_{\text{angle}}}{\alpha^2 + b_{\text{angle}}\alpha + c_{\text{angle}}}$$

where $a_{\text{angle}} = 0.1019$, $b_{\text{angle}} = -0.1953$ and $c_{\text{angle}} = 0.2369$.

Now, when modeling the connectivity graph, we want to calculate the probability of two particles being connected. However, up to now, we only have three

(conditional) probabilites given the area of facet, distance and angle, respectively. If we just multiply them, the resulting probability is too small. This is why we include a correction factor $c > 0$ and set the probability of two particles being connected to

$$P(a, d, \alpha) = \max\{c \cdot P_{\text{area}}(a) \cdot P_{\text{dist}}(d) \cdot P_{\text{angle}}(\alpha), 1\}, \tag{1}$$

where $a$ is the area of the Laguerre facet between two points, $d$ is their distance and $\alpha$ the angle between them with respect to a horizontal plane. The factor $c$ is estimated using the minimum contrast method with respect to the mean coordination number, i.e., the mean number of edges emanating from a vertex. This means, we minimize the cost function

$$h(c) = |c_{\text{exp}} - c_{\text{sim}}(c)|,$$

where $c_{\text{exp}}$ is the mean coordination number in the real data set (which was found to be 3.67), and $c_{sim}(c)$ is the mean coordination number of a realization of the model with parameter $c$. Here, $c_{\text{sim}}(c)$ is estimated by generating 100 realizations of the graph model, computing the mean coordination number for each realization and averaging over all of them. The minimization is carried out using the Nelder-Mead algorithm, see [30], with initial parameter $c_0 = 10$. This results in the estimated value of $\widehat{c} = 11.83$.

Note that it would also be possible to estimate the joint probability distribution, given $a$, $d$ and $\alpha$. However, when performing virtual materials testing, by the approach we use, it is easier to vary specific characteristics, i.e., to change only the dependence on area, distance or angle with respect to a horizontal plane.

Now, using Equation (1), we can construct the connectivity graph for the marked point pattern $\mathcal{S}_1$. To ensure complete connectivity, we start with a minimum spanning tree, i.e., a graph that is completely connected. This is done as follows. We construct a graph $G'$ with vertex set $\mathcal{V} = \mathcal{S}_1$ and set of marked edges $\mathcal{E}' \subset (\mathcal{S}_1 \times \mathcal{S}_1, \mathbb{R}_+)$. Thereby it holds $((S_i, R_i), (S_j, R_j), 1/P(A_{i,j}, D_{i,j}, \alpha_{i,j})) \in \mathcal{E}'$ if $F'_{i,j} \neq \emptyset$, where $A_{i,j}$ is the area of $F'_{i,j}$, $D_{i,j}$ is the Euclidean distance be-

tween $S_i$ and $S_j$ and $\alpha_{i,j}$ the horizontal angle between $S_i$ and $S_j$. This means, an edge is added to $\mathcal{E}'$ if there is a Laguerre facet in $\mathcal{T}'$ between the corresponding points and it is marked with the inverse of the probability of these two vertices being connected according to (1). Then Prim's algorithm [31] is used to compute a minimum spanning tree $G$ based on the weighted graph $G'$, i.e., if we interpret the mark of each edge as a cost, $G$ is the completely connected graph (i.e., there is a path from each vertex to every other vertex) with minimal sum of edge costs. Note that this means that those edges that are contained in the minimum spanning tree are the ones that have a high probability according to (1). Let $\mathcal{E}$ be the edge set of $G$. So far, there are still too less edges in the graph (compared to the one extracted from real data). Thus, we add each edge $((S_i, R_i), (S_j, R_j), 1/P(A_{i,j}, D_{i,j}, \alpha_{i,j})) \in \mathcal{E}'\backslash\mathcal{E}$ to $\mathcal{E}$ with probability $P(A_{i,j}, D_{i,j}, \alpha_{i,j})$, leading to the final connectivity graph $G = (\mathcal{V}, \mathcal{E})$, which ressembles the structural characteristics of the connectivity graph extracted from real data, in particular the mean coordination number. Note that the marks of the edges in $\mathcal{E}$ can be discarded (as they were only needed for the minimum spanning tree and its completion). Thus, to make notation simpler, instead of $((S_i, R_i), (S_j, R_j), 1/P(A_{i,j}, D_{i,j}, \alpha_{i,j})) \in \mathcal{E}$ we just shortly write $(S_i, S_j) \in \mathcal{E}$ in the following sections.

### *3.3. Insertion of empty polytopes*

In this section, we explain in detail how empty polytopes are added to the Laguerre tessellation $\mathcal{T}'$. As already said, they are important to ensure the lower volume fraction of the material. The polytopes into which we will put particles should not be too much larger than the corresponding particles, because otherwise the connectivity constraints cannot be achieved with reasonably shaped particles. However, we have to ensure that the empty polytopes we add do not destroy Laguerre facets where connectivity is indicated by the connectivity graph. This is the reason why the following procedure is chosen.

To begin with, we compute the set of centroids $\{S'_k\}$ of the Laguerre facets

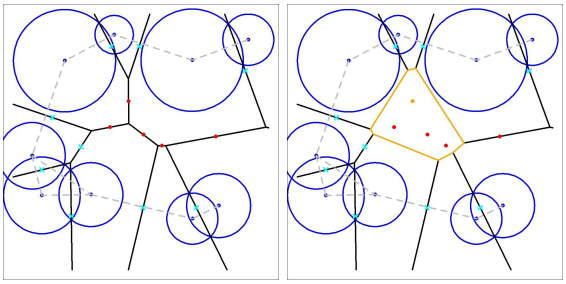

(a) (b)

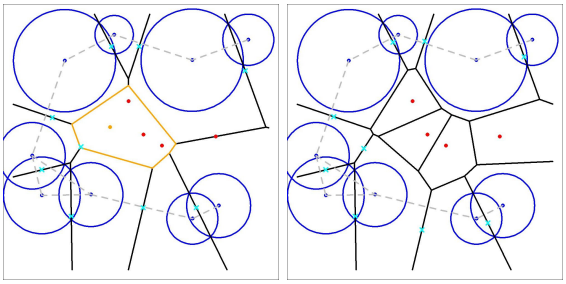

(c) (d)

Figure 7: Addition of empty polytopes to the tessellation. (a) Candidates for generators of empty polytopes $\{S_k''\}$ (red) are computed as barycenters of Laguerre facets where the connectivity graph does not indicate connectivity of particles. Centers of facets with indicated connectivity are called $\{S_k'\}$ and marked in lightblue. The mark of each possible generator point of an empty polytope is chosen to be zero. (b) For each possible generator $S_{k_0}''$, it is checked if the corresponding Laguerre polytope (with respect to the point pattern $\mathcal{S}_1 \cup S_{k_0}''$) covers a point in $\{S_k'\}$. If not, the generator is kept, otherwise it is deleted. (c) Here, a point belonging to $\{S_k'\}$ is covered by a Laguerre polytope (yellow), so the corresponding generator is not kept. (d) Final set of generators for empty polytopes (red) with corresponding tessellation.

$F'_{ij}$ for which an edge between $S_i$ and $S_j$ exists in the connectivity graph, i.e.,

$$\{S'_k\} = \{\bar{F}'_{ij},\, (S_i, S_j) \in \mathcal{E}\},$$

where $\bar{F}'_{ij}$ is the centroid of the facet $F'_{ij}$, and $\mathcal{E}$ is the edge set of the connectivity graph $G$. Furthermore, we consider the set of possible generators of empty polytopes

$$\{S''_k\} = \{\bar{F}'_{ij},\, (S_i, S_j) \notin \mathcal{E}, F'_{ij} \neq \emptyset\},$$

i.e., the centroids of all facets where no contact of the corresponding pair of particles is indicated by the connectivity graph. The set $\{S'_k\}$ is shown as lightblue crosses and $\{S''_k\}$ as red dots in Figure 7(a). Then, for being able to compute a Laguerre tessellation, each point $S''_k$ has to be assigned a mark $R''_k$, resulting in a marked point pattern $\{(S''_k, R''_k)\}$. All marks are chosen to be $R''_k = 0$. Now, in order to ensure that (reasonable) connections of particles are possible where the connectivity graph indicates so, we thin out the set of possible generators of empty polytopes $\{(S''_k, R''_k)\}$ such that no point $\{S'_k\}$ is covered by an empty polytope. This means that, for each candidate $(S''_{k_0}, R''_{k_0})$, we consider the tessellation $\mathcal{T}_{k_0}$ induced by the point pattern $\{\mathcal{S}_1 \cup (S''_{k_0}, R''_{k_0})\}$. Recall that $\mathcal{S}_1$ is the system of particle locations (and marks) defined in Section 3.1. If the polytope $P''_{k_0} \in \mathcal{T}_{k_0}$ induced by $(S''_{k_0}, R''_{k_0})$ contains a point from $\{S'_k\}$, the candidate $(S''_{k_0}, R''_{k_0})$ is rejected. Otherwise, it is accepted and added to the final set of generators of empty polytopes, which will be denoted by $\mathcal{S}_2$. In Figure 7(b), a candidate is shown that is accepted (yellow dot), because there is no point of $\{S'_k\}$ (lightblue crosses) in the corresponding polytope $P''_{k_0}$ (yellow). On the other hand, in Figure 7(c), a candidate is shown which is not accepted. The final set $\mathcal{S}_2$ of generators of empty polytopes together with the set of particle positions $\mathcal{S}_1$ and the corresponding tessellation $\mathcal{T}$ induced by $\mathcal{S}_1 \cup \mathcal{S}_2$ is shown in Figure 7(d).

### *3.4. Modeling of particles*

Given the final tessellation $\mathcal{T}$ on the sampling window $\widetilde{W}$, we now can place particles into each polytope in $\mathcal{T}$ that is induced by a point from $\mathcal{S}_1$. The

polytopes induced by points from $\mathcal{S}_2$ remain empty, ensuring the overall lower volume fraction. Thus, let $\{P_i,\ S_i \in \mathcal{S}_1\}$ be the set of polytopes in $\mathcal{T}$ induced by the points from $\mathcal{S}_1$. In this section, we describe how a particle can be modelled in each of these polytopes. The approach is adapted from [16]. The idea of modeling particles via spherical harmonics is shortly revised in the following.

*3.4.1. Description of particles using spherical harmonics*

Each particle is considered as a realization of a so-called Gaussian random field $\psi : [0, \pi] \times [0, 2\pi] \to \mathbb{R}$ on the sphere, where for each angle $(\theta, \phi)$ the corresponding value $\psi(\theta, \phi)$ describes the distance from the centroid of the particle to its boundary in direction $(\theta, \phi)$. Note that, in order to do so, we need to assume that particles are star-shaped, which is typically the case in the real data set. The Gaussian random field $\psi$ is uniquely determined by its mean radius $\mu$ and its so-called angular power function $A : [0, \infty) \to [0, \infty)$, which controls the shape of the surface. We make use of a special representation of Gaussian random fields, where we assume that the values of $A : [0, \infty) \to [0, \infty)$ can be given in a certain parametric form, see Section 3.4.2, considering spherical harmonic functions. To define them, we need the following two definitions. First, the Legendre polynomial $P_l : [-1, 1] \to \mathbb{R}$ for $l \in \mathbb{N}_0$, which is defined as

$$P_l(x) = 2^{-l} \frac{1}{l!} \frac{\mathrm{d}^l}{\mathrm{d}x^l} (x^2 - 1)^l.$$

Given this definition, we can introduce the associated Legendre functions $P_{l,m} : [-1, 1] \to \mathbb{R}$ for $l \in \mathbb{N}_0$ and $m \in \{0, ..., l\}$, which are given by

$$P_{l,m}(x) = (-1)^m (1 - x^2)^{m/2} \frac{\mathrm{d}^m}{\mathrm{d}x^m} P_l(x).$$

The spherical harmonic functions $Y_{l,m} : [0, \pi] \times [0, 2\pi) \to \mathbb{C}$ for $l \in \mathbb{N}_0$ and $m \in \{0, .., l\}$ are then defined via

$$Y_{l,m}(\theta, \phi) = \sqrt{\frac{(2l + 1)(l - m)!}{4\pi(l + m)!}} P_{l,m}(cos(\theta)) e^{im\phi}.$$

More details can be found in [32].

Based on these defintions, a Gaussian random field with mean radius $\mu$ and angular power function $A : [0, \infty) \to [0, \infty)$ can be represented as a series expansion with respect to spherical harmonic functions. We still define the angular power spectrum $(A_l)_{l=0}^{\infty}$ with $A_l = A(l)$ for $l \in \mathbb{N}_0$. Given this, the Gaussian random field can be represented by

$$\psi(\theta, \phi) = \sum_{l=0}^{\infty} a_{l,0} Y_{l,0}(\theta, \phi) + 2 \sum_{m=1}^{l} \mathrm{Re}(a_{l,m}) \mathrm{Re}(Y_{l,m}(\theta, \phi)) - \mathrm{Im}(a_{l,m}) \mathrm{Im}(Y_{l,m}(\theta, \phi)),$$

with $a_{0,0} \sim N(\mu, A_0)$, $a_{l,0} \sim N(0, A_l)$ for $l > 0$, $\mathrm{Re}(a_{l,m}) \sim N(0, A_l/2)$ and $\mathrm{Im}(a_l, m) \sim N(0, A_l/2)$ for $l \in \mathbb{N}$, $m \in \{1, ..., l\}$. For practical applications, it is possible to truncate the first sum at a parameter $L$, because for large indices $l \in \mathbb{N}$ the contribution of the corresponding spherical harmonic functions is small. Thus we have

$$\psi(\theta, \phi) \approx \sum_{l=0}^{L} a_{l,0} Y_{l,0}(\theta, \phi) + 2 \sum_{m=1}^{l} \mathrm{Re}(a_{l,m}) \mathrm{Re}(Y_{l,m}(\theta, \phi)) - \mathrm{Im}(a_{l,m}) \mathrm{Im}(Y_{l,m}(\theta, \phi)),$$

for some $L \in \mathbb{N}$.

Note that the $Y_{l,m}$ are fixed, i.e., the only free variables are the $a_{l,m}$, which follow a multivariate normal distribution determined by the mean radius $\mu$ and the angular power spectrum $(A_l)_{l=0}^{L}$. Thus, for the realization of a particle, we only need a realization of a multivariate normal distribution for each polytope we want to place a particle into. For this purpose, we need to estimate the angular power spectrum and determine the mean radius for each particle as well as to include conditions for particles such that they are connected according to the connectivity graph. This will be explained in the following sections.

*3.4.2. Estimation of the angular power function*

To estimate the distributions of the coefficients in the series expansion of $\psi(\theta, \varphi)$, we describe each particle of the real data set by a spherical harmonics approximation. To do so, the approach proposed in [17] is used. Given the coefficients $a_{l,m}$ for each particle, we can estimate the variances of the corresponding normal distributions, i.e., we get estimates for $A_l$, $l = 1, ..., L$, see black dots in Figure 8. Based on these estimates, we fit a parametric function to get an

estimate for the angular power function. We choose the same type of parametric function as in [16], i.e.,

$$A(l) = \frac{a_{\text{apf}} l + b_{\text{apf}}}{l^2 + c_{\text{apf}} l + d_{\text{apf}}},$$

and the fitting procedure results in $a_{\text{apf}} = 0.615$, $b_{\text{apf}} = 0.0466$, $c_{\text{apf}} = -3.642$ and $d_{\text{apf}} = 3.398$. The estimated angular power function is shown in Figure 8.

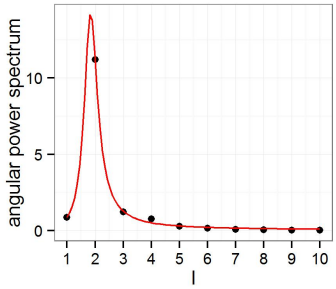


Figure 8: Estimated angular power function. Black dots: Estimates of the angular power spectrum; Red line: Fitted angular power function.

*3.4.3. Determining the mean radius of each particle*

Recall that we place a particle into each polytope that is induced by a point in $\mathcal{S}_1$, and that there are empty polytopes induced by the points in $\mathcal{S}_2$. The overall volume fraction of the particle phase in the real data is $V_{\text{exp}} = 0.4157$. Let $\xi$ be the volume fraction of polytopes induced by points from $\mathcal{S}_1$, i.e., to be filled with particles. To match the overall volume fraction $V_{\text{exp}}$ of the particle phase on average, each particle has to cover a fraction of $V_{\text{exp}}/\xi$ of its corresponding polytope. This is achieved by setting the variable $a_{0,0}$ introduced in Section 3.4.1 for each polytope $P_i$ to a constant, which depends on the corresponding polytope. Given the estimate of the angular power spectrum stated in Section 3.4.2, it can be shown that (under the assumption of independence of the coefficients $a_{ij}$), it holds for the expected volume $\mathbb{E}V$ of a particle that

$$\mathbb{E}V \approx 0.09403 a_{0,0}^3 + 24.5567 a_{0,0}. \tag{2}$$

Thus, for each polytope $P_i$ with volume $|P_i|$ we solve

$$\rho|P_i|V_{\exp}/\xi = 0.09403a_{0,0}^3 + 24.5567a_{0,0}. \tag{3}$$

for $a_{0,0}$, where $\rho$ is an adjustment factor that corrects for errors that occur because Equation (2) only holds for independent coefficients $a_{ij}$. However, this is not the case if we include conditions induced by the connectivity graph, see Section 3.4.4 below. Then, for the simulation of each particle, $a_{0,0}$ is chosen as the solution of (3).

The adjustment factor $\rho$ is fitted using the Nelder-Mead algorithm, comparing the mean volume fraction of the particle phase in simulated data with that of the real data set. The mean volume fraction of the particle phase of the simulated data set was estimated as the mean of 8 realizations of the model (as this could easily be done in parallel). An initial value of $\rho_0 = 0.9$ was used for the optimization. This results in $\rho = 0.875$.

*3.4.4. Incorporating connectivity conditions for particles*

By the methodology described up to now, we can place a particle into each polytope $P_i$ induced by points from $\mathcal{S}_1$. It is centered at the barycenter of the polytope, its shape corresponds statistically to the shape of particles in the real data set and its volume can be regulated such that the overall volume fraction of particles fits to the volume fraction of the real data. However, what is also important, is to ensure complete connectedness of particles according to the connectivity graph. This is done as follows. For each polytope $P_i$ in $\mathcal{T}$ induced by a marked point $(S_i, R_i) \in \mathcal{S}_1$ we consider the set of all facets

$$\mathcal{F}_i = \{F_{i,j},\, (S_i, S_j) \in \mathcal{E}\},$$

where $\mathcal{E}$ is the edge set of the connectivity graph $G$ and $F_{i,j}$ is the facet between the polytopes $P_i$ and $P_j$ in $\mathcal{T}$. Note that $\mathcal{F}_i$ contains those facets of the polytope $P_i$ that correspond to a neighboring polytope where connectivity is indicated by the connectivity graph. Such a facet is sketched in Figure 9. To ensure that particles touch each other, we simply choose points on the facets

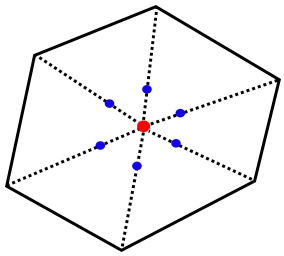

Figure 9: Laguerre facet and points that particles in both of the corresponding polytopes have to touch.

$\mathcal{F}_i$ that the particle in the polytope $P_i$ has to touch. If the connectivity graph indicates a connection between particles in polytope $P_i$ and $P_j$, and both particles have to touch the same points on $F_{i,j}$, then they automatically touch each other, ensuring connectivity. The points on each facet are chosen as the center of the facet (red point in Figure 9) and points at a proportion of 0.15 from the center of the facet to its vertices (blue points in Figure 9). We call the points that a particle has to touch the constraints. Recall that a particle described by spherical harmonics can be realized by drawing a realization from a multivariate normal distribution. Due to that fact, a spherical harmonics particle with constraints can be generated by drawing a realization from a conditional multivariate normal distribution. For details and implementation techniques, we refer to [16].

We have already accounted for two specifications of the data set considered in the present paper - the lower volume fraction and the anisotropic structure. What still has to be done, is to find a method to deal with the very irregular particle shapes, indicated by the large peak of the angular power function (e.g., compared to that one which has been considered in [16]). Due to this, the so-called Gibbs phenomenon or ringing occurs [33], i.e., we observe unintended oscillations on the particle surface. The Gibbs phenomenon can be avoided by using a smaller parameter $L$. We found that for $L = 10$ no problems regarding ringing occur, while the shape of the particles is still described very well, including structural details. However, the number of constraints (i.e., points

the particle has to touch), is limited by the parameter $L$, where the maximum number of constraints is $(L+1)^2 - 1$, but already for a smaller number of constraints highly atypical and degenerate particles might be generated. Those particles can easily be identified, because they typically stick out considerably of their polytopes. We solve this problem by using dynamical connectivity conditions for particles. That means, if a particle is degenerate, we remove one of the constraints, and again sample from a multivariate normal distribution, with one fewer constraint. Thereby the constraints given by the facet centers (red point in Figure 9) are never removed, which ensures that particles will still be connected with probability 1. Furthermore, we always remove the constraint with the minimum distance to another constraint, which ensures that the general structure of connections of particles is kept as good as possible. A particle is thereby identified as degenerate if its maximum distance from the center to the surface is larger than 1.5 times the maximum distance of the center of the polytope to its surface (which exactly means the particle sticks out considerably of the polytope). In case there is no further constraint that can be removed, a new point pattern and connectivity graph is realized.

For more information concerning the Gibbs phenomenon, we refer to [33].

*3.4.5. Morphological smoothing*

Finally, we discard the tessellation and the graph and end up with a connected particle system. In order to smooth the boundary between neighboring particles, in a last step, a morphological smoothing is performed, i.e., we perform a morphological closing with radius $r = 2$, see [19].

## 4. Validation

In this section, we describe the validation of our model using characteristics of point processes and random graphs as well as further morphological image characteristics. To begin with, the point pattern model for the positions and approximate sizes of particles is validated in Section 4.1. Then, the graph model for particle connectivity is compared to the particle connectivity in the real data

set, see Section 4.2. In Section 4.3, the final output of the model is validated using various morphological image characteristics. All validation steps are based on 12 realizations of the model, compared to 12 disjoint cutouts of the real data set, each of which has a size of $400 \times 400 \times 109$ voxels, i.e., $176 \times 176 \times 47.96\mu m^3$. This is a reasonable sample size that gives enough information about the structure while still being practible regarding runtime and memory. We use 12 realizations because this is the maximum number of disjoint cutouts of this size that can be taken from the real data set. Analysis of the variances of different characteristics indicates that this number of samples allows reliable statements regarding the fit.

### *4.1. Marked point pattern*

To begin with, we analyze the goodness of fit of the marked point pattern model introduced in Section 3.1 to the point pattern induced by the particle positions and sizes in the real data set. Note that the most important characteristics, the intensity of points and the distribution of marks, have been fitted directly to real data. However, to indicate that the model fits the structural properties of real data, we consider four further point-process characteristics. First, we look at the nearest neighbor distance distribution function. This function describes the probability of a randomly chosen point of the point pattern to have its closest neighbor within given distances. For detailed information, we refer to [34]. In Figure 10(a) the estimated nearest neighbor distance distribution function for the realizations of the model (red) is shown and compared to that one obtained from the the cutouts of the real data set (blue), where shaded areas describe the range between the pointwise estimated 5% and 95% quantiles. We can observe a slight difference between the results obtained from the model and the real data sets for small distances, but the general structural properties are resembled by the model.

Recall that the point pattern model is only an auxiliary tool - what we really need are the polytopes of the Laguerre tessellation induced by this marked point pattern. This is why for validation purposes, we consider characteristics of these

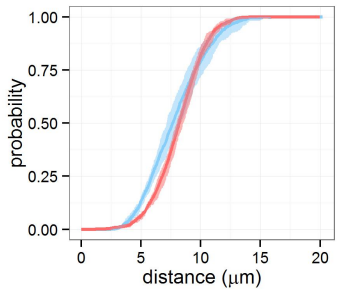


(a) Nearest neighbor distance distribution function.

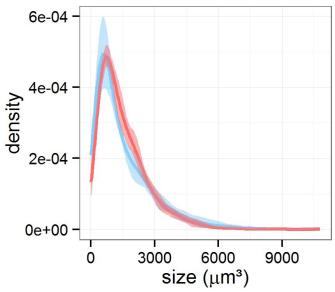


(b) Size of Laguerre polytopes.

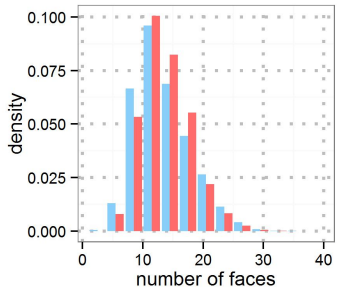


(c) Number of Laguerre facets per polytope.

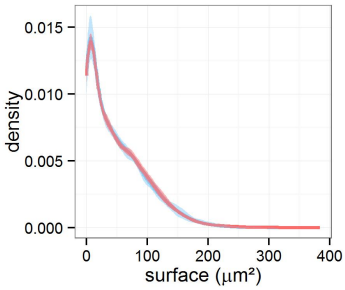


(d) Area of Laguerre facets.

Figure 10: Characteristics of marked point patterns describing positions and sizes of particles. Blue: Real data sets; Red: Simulations. Shaded areas show the range between the estimated 5% and 95% quantiles.

polytopes. Figure 10(b) shows the size distribution of the Laguerre polytopes. In Figure 10(c) we can see a histogram showing the number of Laguerre facets per polytope. Furthermore (as it is needed for modeling the connectivity graph) the surface area of the polytopes is investigated - a comparison of results obtained for model and real data is shown in Figure 10(d). All these characteristics show a good accordance of results obtained for real and simulated data, respectively.

### *4.2. Connectivity graph*

In this section, we compare the connectivity graph induced by the particles in the real data sets to realizations of the graph drawn from our model. For a visual impression, we refer to Figure 11. It can be seen that the basic structural properties are quite similar, and that the anisotropy is nicely resembled by the model.

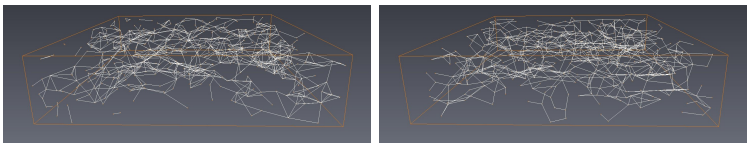

(a) Real data set. (b) Corresponding simulation.

Figure 11: Comparison of the connectivity graph for a cutout of the real data set and corresponding simulation. Lines indicate connectivity between corresponding particles.

To validate the graph model more formally, we consider two graph characteristics. To begin with, we look at the distribution of the coordination number, i.e., the number of outgoing edges from each vertex. The corresponding histograms are shown in Figure 12(a). Note that the mean coordination number has been fitted in the course of parameter estimation, but also the entire distribution nicely fits to the real data set. To also ensure that the model reflects the anisotropic structure of the real data set, we consider the distribution of angles between connected vertices with respect to a horizontal plane, see Figure 12(b). An almost perfect agreement with the real data sets can be found.

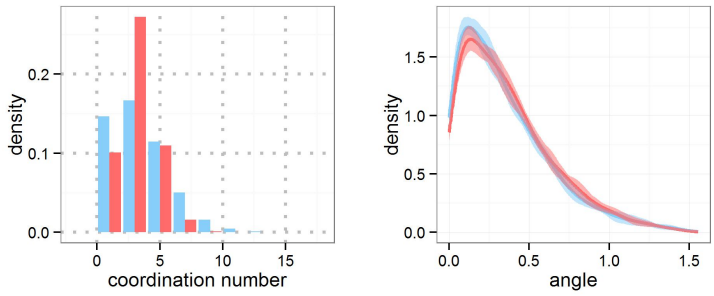


(a) Coordination number.

(b) Angle between two connected vertices with respect to a horizontal plane.

Figure 12: Characteristics of the graph model describing particle connectivity. Blue: Real data sets; Red: Simulations. Shaded areas show the range between the estimated 5% and 95% quantiles.

### *4.3. Particle system*

Having shown that the auxiliary tools, i.e., marked point pattern and connectivity graph, nicely correspond to the real data set, we now want to validate the entire structure, i.e., the completely connected union of particles. In Figure 13, a cutout of the real data set is compared to a realization of the model with the same size. We observe a nice structural accordance. Particles in simulated and real data look very similar and the anisotropic structure is resembled by the model, i.e., particles are also tendentially stretched in horizontal direction.

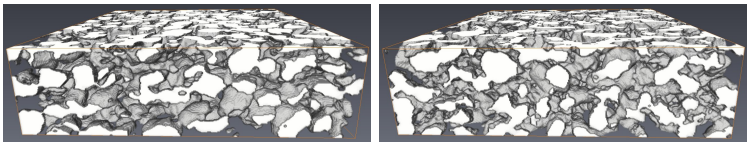

(a) Real data set.

(b) Corresponding simulation.

Figure 13: Comparison of a cutout of the real data set and a corresponding simulated microstructure.

Of course, we also perform a more formal validation for the complete system of particles. To begin with, we look at simple characteristics, where the most

important ones are volume fraction and specific surface area. In Table 1 we see that there is hardly any difference in volume fraction of the particle phase between real data sets and simulations (as the volume fraction can be exactly adjusted in the model). Also the specific surface area fits nicely with a small error of only about 1%. In Figure 14, boxplots of the volume fractions and

Table 1: Comparison of volume fraction and specific surface area for real and simulated data sets.

| | real | simulation | relative error |
|---|---|---|---|
| volume fraction | 0.41483 | 0.41475 | 0.02% |
| specific surface area (1/µm) | 0.19681 | 0.19907 | 1.15% |

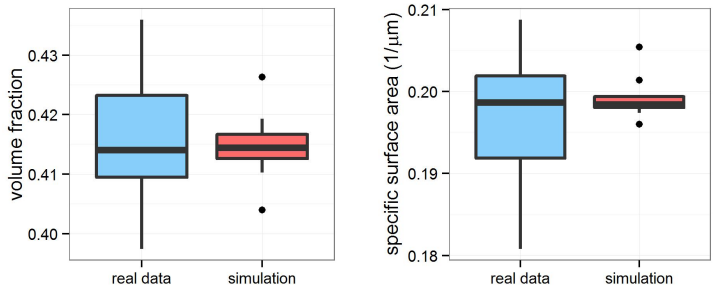


(a) Volume fraction. (b) Specific surface area.

Figure 14: Volume fraction and specific surface area of the particle system. Blue: Real data sets; Red: Simulations. Shaded areas show the range between the estimated 5% and 95% quantiles.

surface areas for the 12 cutouts of the real data set and 12 simulations are shown, which indicate that the variance of these characteristics in the model is smaller than in the real data sets.

Of course, we do not only validate the model regarding simple characteristics like volume fraction and specific surface area, but also want to investigate the structural fit of the model. To do so, we consider further morphological image characteristics. First, we look at the so-called chord length distribution function

$C_d : [0, \infty) \to [0, 1]$, which can be interpreted as follows. If one puts a random line in direction $d$ into an image with a solid phase and a void phase, there are segments of intersection with the solid phase, which we call chords. Then, $C_d(l)$ is the probability that the length of a chord (chosen at random) is not larger than $l$. For further details regarding chord length distributions, we refer to [35]. In Figure 15, the estimated chord length distribution functions for real data and corresponding simulations are shown, where we consider the vertical direction (green curve) and two perpendicular horizontal directions (yellow and orange curves). The plot on the left-hand side clearly shows that the chord lengths in vertical direction are tendentially shorter than with respect to both horizontal directions, which results from the anisotropic structure of the particle phase. The plot on the right-hand side shows that this feature is nicely resembled by the model, i.e., the chord length distribution function shows that anisotropy is captured by the model.

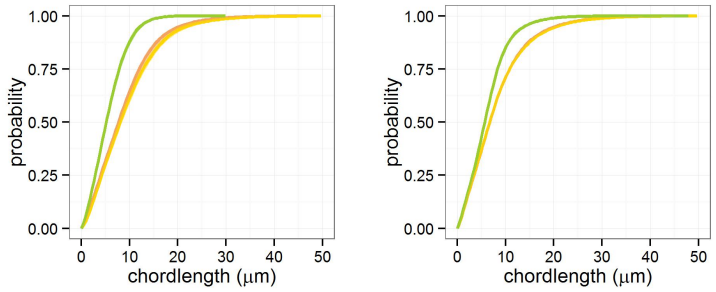


(a) Real data sets. (b) Simulated structures.

Figure 15: Chord length distribution functions. Green: Vertical direction; Yellow and orange: Perpendicular horizontal directions.

The chord length distribution function gives us information regarding the structural fit of the simulated particle system to the one extracted from tomographic images. Of course, in battery applications, also the structural properties of the pore phase are very important. The so-called continuous pore size distribution function [36] is a suitable tool for the comparison of structural properties

of the pore space. The value of the continuous pore size distribution function for a radius $r$ gives us the volume fraction of the subset of the pore phase that can be covered by spheres with radius $r$ that are completely contained in the pore phase, i.e., that do not overlap with particles. For further background regarding the continuous pore size distribution information, we refer to [36]. Estimates of the continuous pore size distribution functions for real and simulated data are visualized in Figure 16(a). The curves are in good accordance, where the pointwise estimated 5% and 95% quantiles of the estimated continuous pore size distribution for the simulated data do not exceed the corresponding quantiles of the real data sets.

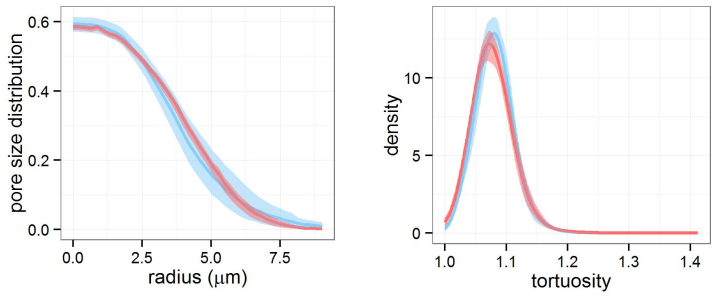


(a) Continuous pore size distribution. (b) Geodesic tortuosity.

Figure 16: Continuous pore size distribution and geodesic tortuosity of the pore phase. Blue: Real data sets; Red: Simulations. Shaded areas show the range between the estimated 5% and 95% quantiles.

Finally, we consider a further morphological characteristic that is important for transport processes, the geodesic tortuosity [14]. This means, we look at the ratio between the lengths of shortest paths from bottom to top through the pore phase of the material, divided by the material thickness. Histograms of the corresponding estimates for real and simulated data can be found in Figure 16(b). Again, an excellent fit can be observed.

## 5. Outlook

In the previous sections, we have dealt with the construction and validation of a parametric 3D microstructure model for the morphology of lithium-ion power cell anodes. We now want to give an outlook towards virtual materials testing, which can be based on this model. The two main abilites needed for virtual materials testing of battery electrodes are 1) a microstructure generator that is able to provide virtual electrode morphologies and 2) a possiblity to analyze the electrochemical performance of geometrically complex microstructures on the computer. In Section 5.1, we show how the model presented in this paper can be used to generate virtual structures with various morphological properties. In Section 5.2, we briefly discuss how the software given in [37] can be used to gain information about the electrochemical performance of electrode microstructures on the computer. To give a simple example, we compute the cell potential over time for tomographic image data as well as corresponding microstructures simulated by our model.

### *5.1. Generation of further virtual structures*

In this section, we show that the model described in the present paper can be used to generate further virtual, but still realistic microstructures, the morphological properties of which differ from those of the real data set. This can be done by systematically varying model parameters. Examples of possible modifications are given in Figure 17. For instance, we can change simple structural features like volume fraction (top left) by changing the corresponding model parameter. By changing the connection probabilites in the graph model, we can stronger pronounce the anisotropy (top right) or create structures without anisotropy effects (bottom left). Furthermore, we can realize virtual morphologies with structural gradients, see the image on the bottom right of Figure 17, where the volume fraction of the particle phase decreases from bottom to top.

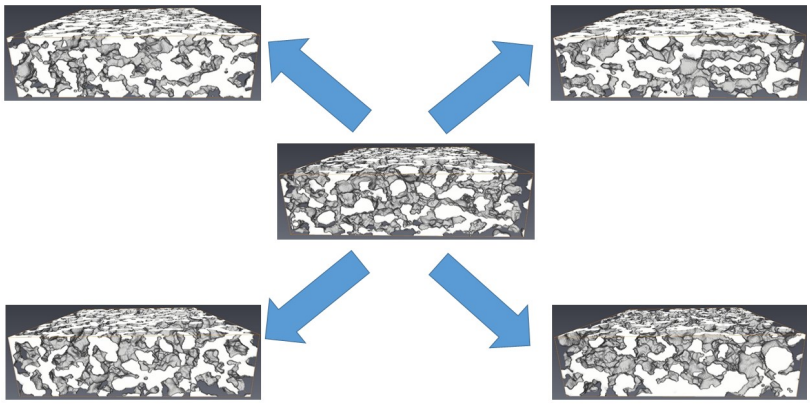

Figure 17: Virtual structures with various (modified) mophological properties. Center: Structure fitted to the real data; Top left: Higher volume fraction of particle phase; Top right: Structure with more pronounced anisotropy; Bottom left: Structure without anistropy; Bottom right: Structural gradient, i.e. decreasing volume fraction of particle phase from bottom to top.

### *5.2. Estimation of electrochemical characteristics*

In this section, we briefly describe a tool which makes it possible to analyze the electrochemical performance of virtual microstructures, see [37]. It is based on a finite volume discretization of the thermodynamically consistent transport theory presented in [10] and [38]. Using this software, we can estimate electrochemical properties of anode morphologies gained by tomographic imaging as well as simulated microstructures that do not (yet) exist physically, but only virtually on a computer. In particular, this tool can be used to analyze virtual microstructures like the ones described in Section 5.1. Doing so, one can try to identify microstructures with preferable electrochemical properties. However, this is beyond the scope of the present paper and thus subject of further research. Here, to give a simple example of the procedure, we show how the cell potential over time during lithiation can be estimated for tomographic image data as well as corresponding microstructures simulated by our model.

The setting for the electrochemical simulations is the following. We inves-

tigate half-cell simulations, where we consider lithiation of the cell at a state-of-charge of 50%. After 60 seconds without any current, we apply a current of $0.008\text{A/cm}^2$ ($\approx$ 4C) for 60 seconds, after which, for another 60 seconds, no current is applied. Such a current peak is a reasonable setting for a power cell. As mentioned above, to give an example, we compute the resulting cell potential over time. The corresponding results are visualized in Figure 18 for the tomographic image data as well as the simulated microstructures that have also been used for model validation in Section 4. It can be seen that the mean value

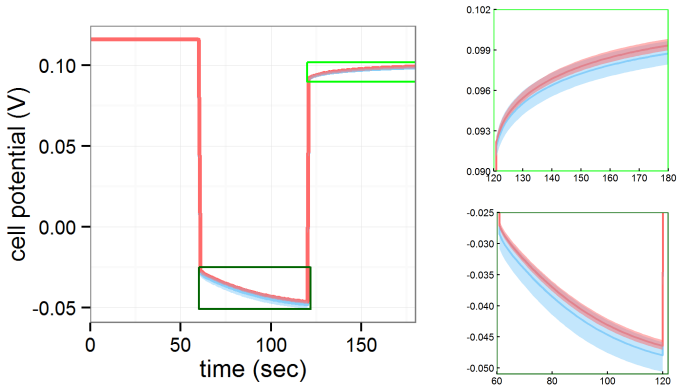


Figure 18: Cell potential over time. Blue: Real data sets; Red: Simulation. Shaded areas show pointwise 95%-confidence intervals. On the right-hand side a zoom is shown to the regions marked by light-green and dark-green boxes, respectively.

of the cell potential of the simulated data sets approximately matches the cell potential of the real data sets for each time step, while the variability of the results obtained for the real data sets is larger than the one for the simulated data sets. The pointwise 95% confidence intervals of the results for the simulated data sets are almost contained within the ones for the experimental data sets for any time step.

## 6. Conclusions

In this work, we have introduced a parametric stochastic 3D microstructure model for simulation of the morphology of power cell anodes. The model is

based on a previously published modeling idea (see [16]) and extends this idea to account for the lower volume fraction of the particle phase in power cell anodes and to include the anisotropic structure of this kind of cells which results from the calendering process.

The basic idea of the extended model is to divide the region of interest in convex polytopes and to fill part of these polytopes with particles using so-called spherical harmonics. The remaining polytopes stay empty to account for the lower volume fraction, where nevertheless a complete connection of the particle system is ensured by a connectivity graph that indicates connections of particles. This connectivity graph has an anisotropic structure such that also the resulting particle system has this property.

The model was fitted to real data gained by synchroton tomography and the goodness of fit was investigated using various morphological image characteristics.

Furthermore, we proved the ability of our model to generate further virtual microstructures of battery anodes with a variety of morphological properties. Thus, it was shown that the parametric 3D model introduced in this paper can be used as a microstructure generator for virtual materials. Finally, an example was given which shows how electrochemical properties of simulated morphologies can be estimated on the computer using the software given in [37].

Besides the overall aim to identify morphologies that can help to improve the functionality of new Li-ion batteries, there are still other possible applications of our model. For example, several studies (see, e.g., [39]) showed that local variability of morphological properties has an enormous influence on functionality. In [40], this has been analyzed e.g. for varying local tortuosity. The microstructure model introduced in the present paper can be adapted to generate structures with different local variability of diverse morphological aspects. The influence of this local variability can then be analyzed using electrochemical simulations. Such investigations can help to better understand the relationship between morphology and functionality of battery electrodes, which in turn can help to improve battery performance.

**Acknowledgements**

This work was partially funded by BMBF under grant number 05M13VUA in the programme "Mathematik für Innovationen in Industrie und Dienstleistungen".

## References

[1] M. M. Thackeray, C. Wolverton, E. D. Isaacs, Electrical energy storage for transportation – approaching the limits of, and going beyond, lithium-ion batteries, Energy & Environmental Science 5 (7) (2012) 7854–7863. doi:10.1039/C2EE21892E.

[2] N.-S. Choi, Z. Chen, S. A. Freunberger, X. Ji, Y.-K. Sun, K. Amine, G. Yushin, L. F. Nazar, J. Cho, P. G. Bruce, Challenges facing lithium batteries and electrical double-layer capacitors, Angewandte Chemie International Edition 51 (40) (2012) 9994–10024. doi:10.1002/anie.201201429.

[3] Q. Wang, P. Ping, X. Zhao, G. Chu, J. Sun, C. Chen, Thermal runaway caused fire and explosion of lithium ion battery, Journal of Power Sources 208 (2012) 210–224. doi:10.1016/j.jpowsour.2012.02.038.

[4] A. Barré, B. Deguilhem, S. Grolleau, M. Gérard, F. Suard, D. Riu, A review on lithium-ion battery ageing mechanisms and estimations for automotive applications, Journal of Power Sources 241 (2013) 680–689. doi:10.1016/j.jpowsour.2013.05.040.

[5] V. Etacheri, R. Marom, R. Elazari, G. Salitra, D. Aurbach, Challenges in the development of advanced Li-ion batteries: a review, Energy & Environmental Science 4 (9) (2011) 3243–3262. doi:10.1039/C1EE01598B.

[6] X. Huang, J. Tu, X. Xia, X. Wang, J. Xiang, L. Zhang, Y. Zhou, Morphology effect on the electrochemical performance of NiO films as anodes for lithium ion batteries, Journal of Power Sources 188 (2) (2009) 588–591. doi:10.1016/j.jpowsour.2008.11.111.

[7] A. H. Wiedemann, G. M. Goldin, S. A. Barnett, H. Zhu, R. J. Kee, Effects of three-dimensional cathode microstructure on the performance of lithium-ion battery cathodes, Electrochimica Acta 88 (2013) 580–588. doi:10.1016/j.electacta.2012.10.104.

[8] R. E. García, Y.-M. Chiang, W. Craig Carter, P. Limthongkul, C. M. Bishop, Microstructural modeling and design of rechargeable lithium-ion batteries, Journal of The Electrochemical Society 152 (1) (2005) A255–A263. doi:10.1149/1.1836132.

[9] J. Newman, W. Tiedemann, Porous-electrode theory with battery applications, AIChE Journal 21 (1) (1975) 25–41. doi:10.1002/aic.690210103.

[10] A. Latz, J. Zausch, Thermodynamic consistent transport theory of Li-ion batteries, Journal of Power Sources 196 (6) (2011) 3296–3302. doi:10.1016/j.jpowsour.2010.11.088.

[11] O. Stenzel, H. Hassfeld, R. Thiedmann, L. J. A. Koster, S. D. Oosterhout, S. S. van Bavel, M. M. Wienk, J. Loos, R. A. J. Janssen, V. Schmidt, Spatial modeling of the 3D morphology of hybrid polymer-ZnO solar cells, based on electron tomography data, The Annals of Applied Statistics 5 (3) (2011) 1920–1947. doi:10.1214/11-AOAS468.

[12] G. Gaiselmann, M. Neumann, L. Holzer, T. Hocker, M. R. Prestat, V. Schmidt, Stochastic 3D modeling of $La_{0.6}Sr_{0.4}CoO_{3-\delta}$ cathodes based on structural segmentation of FIB–SEM images, Computational Materials Science 67 (2013) 48–62. doi:10.1016/j.commatsci.2012.08.030.

[13] G. Gaiselmann, M. Neumann, V. Schmidt, O. Pecho, T. Hocker, L. Holzer, Quantitative relationships between microstructure and effective transport properties based on virtual materials testing, AIChE Journal 60 (6) (2014) 1983–1999. doi:10.1002/aic.14416.

[14] O. Stenzel, O. M. Pecho, M. Neumann, V. Schmidt, L. Holzer, Predicting

effective conductivities based on geometric microstructure characteristics, AIChE Journal 62 (5) (2016) 1834–1843. doi:10.1002/aic.15160.

[15] M. Ender, J. Joos, A. Weber, E. Ivers-Tiffée, Anode microstructures from high-energy and high-power lithium-ion cylindrical cells obtained by X-ray nano-tomography, Journal of Power Sources 269 (2014) 912–919. doi:10.1016/j.jpowsour.2014.07.070.

[16] J. Feinauer, T. Brereton, A. Spettl, M. Weber, I. Manke, V. Schmidt, Stochastic 3D modeling of the microstructure of lithium-ion battery anodes via Gaussian random fields on the sphere, Computational Materials Science 109 (2015) 137–146. doi:10.1016/j.commatsci.2015.06.025.

[17] J. Feinauer, A. Spettl, I. Manke, S. Strege, A. Kwade, A. Pott, V. Schmidt, Structural characterization of particle systems using spherical harmonics, Materials Characterization 106 (2015) 123–133. doi:10.1016/j.matchar.2015.05.023.

[18] T. Mitsch, Y. Krämer, J. Feinauer, G. Gaiselmann, H. Markötter, I. Manke, A. Hintennach, V. Schmidt, Preparation and characterization of Li-ion graphite anodes using synchrotron tomography, Materials 7 (6) (2014) 4455–4472. doi:10.3390/ma7064455.

[19] W. Burger, M. J. Burge, Digital Image Processing: An Algorithmic Introduction Using Java, Springer, New York, 2010.

[20] J. Hoshen, R. Kopelman, Percolation and cluster distribution. I. Cluster multiple labeling technique and critical concentration algorithm, Physical Review B 14 (8) (1976) 3438–3445. doi:10.1103/PhysRevB.14.3438.

[21] J. B. T. M. Roerdink, A. Meijster, The watershed transform: Definitions, algorithms and parallelization strategies, Fundamenta informaticae 41 (1,2) (2000) 187–228. doi:10.3233/FI-2000-411207.

[22] A. Spettl, R. Wimmer, T. Werz, M. Heinze, S. Odenbach, C. E. Krill III, V. Schmidt, Stochastic 3D modeling of Ostwald ripening at ultra-high

volume fractions of the coarsening phase, Modelling and Simulation in Materials Science and Engineering 23 (6) (2015) 065001. doi:10.1088/0965-0393/23/6/065001.

[23] C. Lautensack, S. Zuyev, Random Laguerre tessellations, Advances in Applied Probability 40 (3) (2008) 630–650. doi:10.1239/aap/1222868179.

[24] J. Mościński, M. Bargieł, Z. A. Rycerz, P. W. M. Jacobs, The force-biased algorithm for the irregular close packing of equal hard spheres, Molecular Simulation 3 (4) (1989) 201–212. doi:10.1080/08927028908031373.

[25] S. N. Chiu, D. Stoyan, W. S. Kendall, J. Mecke, Stochastic Geometry and its Applications, 3rd Edition, J. Wiley & Sons, Chichester, 2013.

[26] T. Benaglia, D. Chauveau, D. R. Hunter, D. Young, mixtools: An R package for analyzing finite mixture models, Journal of Statistical Software 32 (6) (2009) 1–29. doi:10.18637/jss.v032.i06.

[27] R Core Team, R: A Language and Environment for Statistical Computing, R Foundation for Statistical Computing, Vienna, Austria (2014).

[28] R. Diestel, Graph Theory, Springer, Berlin, 2010.

[29] The Mathworks, Inc., Natick, Massachusetts, MATLAB version 8.1.0.604 (R2013a) (2013).

[30] J. A. Nelder, R. Mead, A simplex method for function minimization, The Computer Journal 7 (4) (1965) 308–313. doi:10.1093/comjnl/7.4.308.

[31] R. C. Prim, Shortest connection networks and some generalizations, Bell System Technical Journal 36 (6) (1957) 1389–1401. doi:10.1002/j.1538-7305.1957.tb01515.x.

[32] A. Lang, C. Schwab, Isotropic Gaussian random fields on the sphere: Regularity, fast simulation and stochastic partial differential equations, Annals of Applied Probability 25 (6) (2015) 3047–3094. doi:10.1214/14-AAP1067.

[33] A. Gelb, The resolution of the Gibbs phenomenon for spherical harmonics, Mathematics of Computation 66 (218) (1997) 699–717. doi:10.1090/S0025-5718-97-00828-4.

[34] J. Illian, A. Penttinen, H. Stoyan, D. Stoyan, Statistical Analysis and Modeling of Spatial Point Patterns, J. Wiley & Sons, Chichester, 2008.

[35] J. Ohser, F. Mücklich, Statistical Analysis of Microstructures in Materials Science, J. Wiley & Sons, Chichester, 2000.

[36] B. Münch, L. Holzer, Contradicting geometrical concepts in pore size analysis attained with electron microscopy and mercury intrusion, Journal of the American Ceramic Society 91 (12) (2008) 4059–4067. doi:10.1111/j.1551-2916.2008.02736.x.

[37] ITWM, BEST - Battery and Electrochemistry Simulation Tool (2014). URL http://itwm.fraunhofer.de/BEST

[38] A. Latz, J. Zausch, Multiscale modeling of lithium ion batteries: thermal aspects, Beilstein Journal of Nanotechnology 6 (2015) 987–1007. doi:10.3762/bjnano.6.102.

[39] S. J. Harris, P. Lu, Effects of inhomogeneities – nanoscale to mesoscale – on the durability of li-ion batteries, The Journal of Physical Chemistry C 117 (13) (2013) 6481–6492. doi:10.1021/jp311431z.

[40] D. Kehrwald, P. R. Shearing, N. P. Brandon, P. K. Sinha, S. J. Harris, Local tortuosity inhomogeneities in a lithium battery composite electrode, Journal of The Electrochemical Society 158 (12) (2011) A1393–A1399. doi:10.1149/2.079112jes.